Journal of Molecular Liquids 409 (2024) 125424

Contents lists available at ScienceDirect

Journal of Molecular Liquids

journal homepage: www.elsevier.com/locate/molliq

Harnessing liquid crystal attributes of near-unit photoluminescent benzothioxanthene photosensitizers: Photophysical profiling in solution, solid state, and polymer matrix embedding

Frederico Duarte [a,b,1], Korentin Morice [c,1], Tatiana Ghanem [c], Darío Puchán Sánchez [c], Philippe Blanchard [c], Clara S. B. Gomes [d], Santiago Herrero [e], Clement Cabanetos [c,*], Cristián Cuerva [e,**], Jose Luis Capelo-Martinez [a,b], Carlos Lodeiro [a,b,***]

[a] BIOSCOPE Research Group, LAQV-REQUIMTE, Chemistry Department, NOVA School of Science and Technology, FCT NOVA, Universidade NOVA de Lisboa, 2829-516 Caparica, Portugal
[b] PROTEOMASS Scientific Society, Praceta Jerónimo Dias, 12, 2ª, Costa de Caparica, 2825-466, Portugal
[c] University of Angers, CNRS, MOLTECH-ANJOU, SFR-MATRIX, F-49000 Angers, France
[d] LAQV-REQUIMTE, Chemistry Department, NOVA School of Science and Technology, FCT NOVA, Universidade NOVA de Lisboa, 2829-516 Caparica, Portugal
[e] MatMoPol Research Group, Department of Inorganic Chemistry, Faculty of Chemical Sciences, Complutense University of Madrid, Ciudad Universitaria, 28040 Madrid, Spain

ARTICLE INFO

Keywords:
Liquid crystals
Benzothioxanthene imide derivatives
Fluorescent materials
Polymers

ABSTRACT

Liquid crystals (LCs) have garnered significant attention for their unique optical and electrical properties, making them promising candidates in various technological applications such as smart displays, sensors, telecommunications, biomedicals or wearable electronics. In this study, we explore the potential of several highly emissive benzothioxanthene imide (BTI) derivatives as LC materials with a focus on their robustness and temperature-stable emission behavior. By tailoring the molecular structure of BTIs, we have accomplished exceptional emissive properties while maintaining the inherent advantages of LCs, such as their self-organizing ability and responsive nature. We describe the formation of enantiotropic liquid crystals whose mesomorphic properties dependent on the nature, length, and position of the side chain. Moreover, we have investigated the thermal stability of their emission spectra over a wide range of temperature, highlighting their potential use in demanding conditions where precise optical performances are critical. Our findings underscore the importance of molecular design in achieving highly emissive LC materials with enhanced robustness and temperature stability, opening new avenues for the use of BTI derivatives.

1. Introduction

As an intermediate phase between the isotropic liquid and the crystalline solid, liquid crystals (LCs) gather the fluidity of a liquid in tandem with anisotropic properties, resulting in the formation of self-assembled structures that originate smectic, nematic or columnar phases, among others. While in the smectic mesophases molecules are self-assembled in a layered arrangement, as in the smectic A (SmA) mesophase in which they are aligned in a perpendicular fashion with respect to the layers, the molecules in the nematic ones also exhibit orientational order but can move freely via axial fluctuations around their position. By contrast, in columnar mesophases they form stacks of parallel columns. [1,2] This phenomenon has attracted considerable research interest triggered by the changes of the optical properties derived from the solid-mesophase phase transition, thus providing utility for the development of liquid crystal displays (LCDs). In recent years, researchers stepped back from the reliance on blacklight, due to the non-emissive properties of LCDs, and instead vowed to overcome

* Corresponding author.
** Corresponding author.
*** Corresponding author at: BIOSCOPE Research Group, LAQV-REQUIMTE, Chemistry Department, NOVA School of Science and Technology, FCT NOVA, Universidade NOVA de Lisboa, 2829-516 Caparica, Portugal.
E-mail addresses: clement.cabanetos@univ-angers.fr (C. Cabanetos), c.cuerva@ucm.es (C. Cuerva), cle@fct.unl.pt (C. Lodeiro).
[1] These authors have been contributed equally for this work.

https://doi.org/10.1016/j.molliq.2024.125424
Received 18 April 2024; Received in revised form 25 May 2024; Accepted 1 July 2024
Available online 6 July 2024
0167-7322/© 2024 The Author(s). Published by Elsevier B.V. This is an open access article under the CC BY-NC-ND license (http://creativecommons.org/licenses/by-nc-nd/4.0/).

these limitations by designing novel fluorescent LCs. This new property paved the way to the successful development of organic light-emitting diodes (OLEDs), optical sensing materials, photovoltaic cells and, more recently, circularly polarized luminescence (CPL) materials [3–8].

However, all these advances can be impaired if a key parameter is not considered on luminescent dyes' applications, *i.e.* high photoluminescence quantum yields. Efficient luminophores incorporation into LCs was achieved by Wenquan Li *et al.*, who reported the synthesis and characterization of a triphenylene-fluorescein-triphenylene trimer bridged by $-C_3H_6-$ and $-C_6H_{12}-$ that self-assemblies on a stable hexagonal columnar mesophase which exhibits high fluorescence quantum yield of *ca.* 0.91 in CH_2Cl_2. Shruti Rani reached the same endeavor by synthesizing a solvatochromic perylene linked to two pentaalkynylbenzene units *via* an alkyl spacer, which shows high fluorescence quantum yield in non-polar solvents and self-assembles in a columnar oblique mesophase [9–11].

In line with the quest of demonstrating LC properties with new fluorescent dyes, Yang Li *et al.* highlighted, in two separate works, the relevance of naphthalimide, and derivatives, through tunable photophysical properties by chemical engineering [12,13]. Both works take advantage of different chiral naphthalimide-based dyes to produce circularly polarized luminescence materials by doping the latter into nematic liquid crystals (E7, N-LCs). A standard white-light-emitting N*-LCs (CIE coordinates: (0.31, 0.33)) was attained by matching at appropriate ratio the blue-red color of two chiral NI-based dyes. On the second work a high luminescence dissymmetry factor (+0.91/-0.98) stemming from an effective chirality transfer and intramolecular electronic coupling from microstructure change of AIE-active isomers was demonstrated [12,13].

Taking into account the great properties of arylene imide compounds, Cabanetos and coworkers recently focused their attention on an overlooked and inexpensive vat dye, namely the benzothioxanthene imide (BTI, Fig. 1) [14,15]. In its most simple form, this dual redox dye [16] was found to combine both a large extinction coefficient in the visible along with near unity emission quantum yields in the yellow-green part of the electromagnetic spectrum [17,18]. Moreover, solely functionalized at the imide position for solubility and/or grafting purposes, the group demonstrated synthetically accessible and selective modifications of its π-conjugated core opening doors to new design principles and tunable optoelectronic properties [19,20]. Upcycled in various applications ranging from organic photovoltaics,[21] light emitting devices [22] or even photodynamic therapy [23,24]. Within this context, and as a further step towards the exploration of this fascinating class of compounds, we report herein the pioneer evaluation of potential luminescence and liquid crystal properties through the synthesis and study of specifically designed derivatives whose structures are illustrated in Fig. 1.

2. Experimental section

2.1. Materials

All reagents and chemicals from commercial sources were used without further purification unless specified. Solvents were dried and purified using standard techniques.

Spectroscopy grade solvents were used for photophysical experiments –tetrahydrofuran (THF), chloroform ($CHCl_3$). Poly(methylmethacrylate), PMMA (MW ~ 350,000, Tg 105 °C), KURARITY^{TM} LA4285 Kurashiki, Okayama, Japan, polymer. The perfluoroalkoxy (PFA) supports for the fabrication of polymer films were purchased to Bohlender Gmbh, Germany. Mili-Q ultrapure water was used in all experiments.

2.2. Instrumentation

Polarized optical microscopy (POM) observations were carried out by using an Olympus BX50 microscope equipped with a Linkam THMS 600 heating stage. The transition temperatures and their associated enthalpy data were determined with a PerkinElmer Pyris 1 differential scanning calorimeter. Samples were hermetically sealed in aluminum

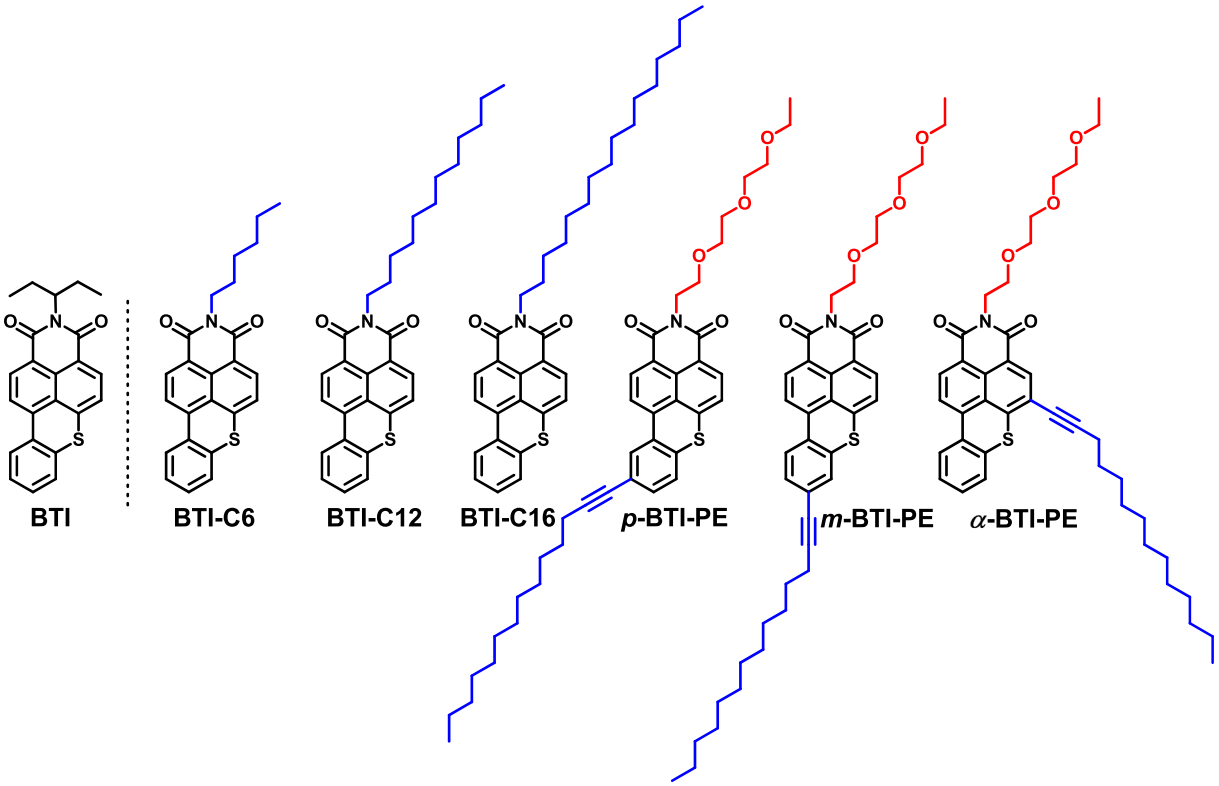

Fig. 1. Structures of BTI and derivatives reported herein, namely **BTI-C6**, **BTI-C12**, **BTI-C16**, ***p*-BTI-PE** ***m*-BTI-PE**, and **α-BTI-PE**.

pans and measurements were carried out with heating and cooling rates of 10 K/min. Temperature-dependent powder X-ray diffraction (XRD) studies were carried out on a Panalytical X'Pert PRO MPD diffractometer with Cu-Kα (1.54 Å) radiation in a θ–θ configuration equipped with an Anton Paar HTK1200 heating stage (X-Ray Diffraction Service at the Complutense University of Madrid).

Flash chromatography was performed with analytical-grade solvents using ALDRICH silica gel (technical grade, pore size 60 Å, 230– 400 mesh particle size). Flexible plates ALUGRAM Xtra SIL G UV254 from MACHEREY-NAGEL were used for thin layer chromatography (TLC). Compounds were detected by UV irradiation (BIOBLOCK SCIENTIFIC). NMR spectra were recorded with a BRUKER AVANCE III 300 (^{1}H, 300 MHz and ^{13}C, 76 MHz) or a BRUKER AVANCE DRX500 (^{1}H, 500 MHz and ^{13}C, 125 MHz). Chemical shifts are given in ppm relative to the residual ^{1}H resonance of the deuterated solvent and coupling constants J in Hz. High resolution mass spectrometry (HRMS) was performed with a JEOL JMS-700B/E. Matrix Assisted Laser Desorption/Ionization was performed on MALDI-TOF MS BIFLEX III Bruker Daltonics spectrometer using DCTB + as matrix (Bruker, Billerica, MA, USA).

The absorption spectra were recorded on a JASCO V-650 UV–Vis Spectrophotometer and the fluorescence emission spectra on a Horiba Jobin-Yvon Scientific Fluoromax-4. Spectra of solid samples were collected with a Horiba-Jobin-Yvon Fluoromax-4® spectrofluorometer using an optic fiber connected to the equipment, by exciting the solid compounds at the appropriated wavelength (nm). A correction for the absorbed light was performed when necessary. Lifetime studies were carried out on TemPro, Deltahub Nanoled of Horiba Jobin-Yvon, with a 390 nm Nanoled. All instruments were provided by PROTEOMASS-BIOSCOPE facility.

Crystals of compounds **BTI-C6** and **BTI-C16** suitable for single-crystal X-ray analysis were selected, covered with Fomblin (polyfluoro ether oil) and mounted on a nylon loop. The data was collected at 150(2) K on a Bruker D8 Venture diffractometer equipped with a Photon II detector and an Oxford CryoSystems Cooler, using graphite monochromated Mo-Kα radiation (λ = 0.71073 Å). The data was processed using the APEX4 suite software package, which includes integration and scaling (SAINT), absorption corrections (SADABS [25]) and space group determination (XPREP). Structure solution and refinement were done using direct methods with the programs SHELXT 2018/2 and SHELXL-2019/2[26,27] inbuilt in APEX and WinGX-Version 2021.3 [28] software packages. All non-hydrogen atoms were refined anisotropically, and all hydrogen atoms were inserted in idealized positions and allowed to refine riding on the parent carbon atom with C–H distances of 0.98 Å, 0.99 Å and 0.95 Å for methyl, methylene and aromatic H atoms, respectively. Both crystalline samples were of poor quality, showing low diffracting power, leading to high R_{int} values, Nevertheless, it was possible to establish the molecular structure of both compounds, agreeing with the obtained through other analytical techniques. The molecular diagrams were drawn with Mercury [29]. Crystal and structure refinement data are given in Table 1. The data was deposited in the CCDC under deposit numbers 2,348,204 for **BTI-C6** and 2,348,205 for **BTI-C16**.

Table 1
Crystallographic experimental data and structure refinement parameters.

	BTI-C6	**BTI-C16**
Formula	$C_{24}H_{21}NO_2S$	$C_{34}H_{41}NO_2S$
M	387.48	527.74
λ (Å)	0.71073	0.71073
T (K)	150(2)	150(2)
crystal system	Triclinic	Triclinic
space group	P-1	P-1
Crystal description	Needle	Needle
Crystal color	Orange	Orange
Crystal Size	0.08 × 0.12 × 0.40	0.06 × 0.12 × 0.40
a (Å)	7.2549(8)	7.326(2)
b (Å)	8.7827(11)	8.219(2)
c (Å)	17.693(2)	25.291(7)
α (deg)	82.847(6)	93.107(10)
β (deg)	78.657(4)	95.881(11)
γ (deg)	69.282(4)	107.864(10)
V (Å^3)	1032.0(2)	1435.8(7)
Z	2	2
ρ_{calc} (g cm^{-3})	1.247	1.221
μ (mm^{-1})	0.176	0.144
θ_{max} (deg)	25.346	25.026
total data	39,423	56,424
unique data	3770	5060
R_{int}	0.2686	0.6672
R [$I > 3\sigma(I)$]	0.1223	0.1852
wR_2	0.2718	0.4006
Goodness of fit	1.075	1.068
ρ min	−0.580	−0.896
ρ max	1.083	1.038

2.3. Synthetic procedures

2.3.1. General procedure for preparation of alky functionalized BTI derivatives BTI-C6, BTI-C12 and BTI-C16

The corresponding alkylamine (1.1 eq) was added to a solution of **BTA** (1 eq) in 2-ethoxyethanol (20 mL/g) before being refluxed overnight. Conversion of the starting material was followed by TLC prior to cool down the reaction mixture and pouring the latter in water. This aqueous phase was extracted with DCM, then the combined organic phases were washed with brine before being dried over $MgSO_4$ and concentrated under vacuum. The resulting solid was finally purified by column chromatography (eluent: DCM) affording the corresponding compound as a bright orange powder in 76 %, 75 % and 78 % yield for **BTI-C6**, **BTI-C12** and **BTI-C16**, respectively.

2-hexyl-1H-thioxantheno [2,1,9-def] isoquinoline-1,3(2H)-dione (BTI-C6): ^{1}H NMR (300 MHz, $CDCl_3$) δ 8.61 (d, J = 8.1 Hz, 1H), 8.42 (d, J = 8.0 Hz, 1H), 8.24 – 8.16 (m, 2H), 7.49 (d, J = 8.0 Hz, 1H), 7.43 – 7.35 (m, 3H), 4.18 (t, J = 7.7 Hz, 2H), 1.79 – 1.66 (m, 2H), 1.48 – 1.38 (m, 2H), 1.38 – 1.29 (m, 4H), 0.90 (t, J = 6.8 Hz, 1H). **^{13}C NMR (126 MHz, $CDCl_3$)** δ 163.84, 163.40, 132.45, 131.64, 130.71, 129.90, 127.57, 126.42, 126.08, 120.34, 119.16, 118.15, 40.53, 31.59, 27.96, 26.85, 22.60, 14.09. **HRMS (MALDI-TOF)**: m/z calcd for $C_{24}H_{21}NO_2S$: 387.1293, found: 387.1288 (Δ= 1.47 ppm).

2-dodecyl-1H-thioxantheno [2,1,9-def] isoquinoline-1,3(2H)-dione (BTI-C12): ^{1}H NMR (500 MHz, $CDCl_3$) δ 8.56 (d, J = 8.1 Hz, 1H), 8.38 (d, J = 7.9 Hz, 1H), 8.17 – 8.14 (m, 1H), 8.13 (d, J = 8.2 Hz, 1H), 7.45 (d, J = 8.0 Hz, 1H), 7.40 – 7.33 (m, 3H), 4.21 – 4.08 (m, 2H), 1.77 – 1.65 (m, 2H), 1.46 – 1.39 (m, 2H), 1.39 – 1.32 (m, 2H), 1.31 – 1.24 (m, 14H), 0.87 (t, J = 6.9 Hz, 3H). **^{13}C NMR (126 MHz, $CDCl_3$)** δ 163.98, 163.54, 140.45, 136.69, 132.58, 131.77, 130.84, 130.44, 130.05, 128.13, 127.71, 126.56, 126.21, 125.62, 121.45, 120.47, 119.29, 118.29, 40.68, 32.06, 29.80, 29.72, 29.55, 29.49, 28.16, 27.33, 22.83, 14.26. **HRMS (MALDI-TOF):** m/z calcd for $C_{30}H_{33}NO_2S$: 471.22281, found: 471.22265 (Δ = 0.34 ppm).

2-hexadecyl-1H-thioxantheno [2,1,9-def] isoquinoline-1,3(2H)-dione (BTI-C16): ^{1}H NMR (500 MHz, $CDCl_3$) δ 8.58 – 8.42 (m, 1H), 8.39 – 8.25 (m, 1H), 8.17 – 7.96 (m, 2H), 7.46 – 7.27 (m, 4H), 4.18 – 4.07 (m, 2H), 1.77 – 1.65 (m, 2H), 1.45 – 1.39 (m, 2H), 1.38 – 1.34 (m, 2H), 1.32 – 1.20 (m, 22H), 0.87 (t, J = 6.8 Hz, 3H). **^{13}C NMR (126 MHz, $CDCl_3$)** δ 163.95, 163.50, 140.42, 132.56, 130.81, 130.03, 127.68, 126.53, 126.18, 121.43, 120.44, 119.26, 40.67, 32.07, 29.85, 29.73, 29.51, 28.16, 27.34, 22.84, 14.27. **HRMS (MALDI-TOF)**: m/z calcd for $C_{34}H_{41}NO_2S$: 527.2856, found: 527.1288 (Δ = 0.61 ppm).

2.3.2. Synthesis of intermediates *BTI-PE* and *α-BTI-Br*

2-(2-(2-(2-ethoxyethoxy)ethoxy)ethyl)-1H-thioxantheno [2,1,9-def] isoquinoline-1,3(2H)-dione (BTI-PE): 2-(2-(2-ethoxyethoxy) ethoxy)ethan-1-amine (160 mg, 0.904 mmol) was added to a solution of **BTA** (250 mg, 0.822 mmol) in 2-ethoxyethanol (20 mL). The mixture was refluxed overnight. Conversion was confirmed by TLC before

pouring the crude in water and extract it from the aqueous phase with DCM. The resulting organic phase was then dried over $MgSO_4$ and evaporated by vacuum pumping. The resulting solid was purified by column chromatography (eluent: DCM/EtOAc 7/3) to afford **BTI-PE** (298 mg, 77 % yield). **^{1}H NMR (300 MHz, $CDCl_3$)** δ 8.56 (d, J = 8.1 Hz, 1H), 8.37 (d, J = 8.0 Hz, 1H), 8.19 – 8.11 (m, 2H), 7.45 (d, J = 8.0 Hz, 1H), 7.42 – 7.34 (m, 3H), 4.42 (t, J = 6.2 Hz, 2H), 3.82 (t, J = 6.2 Hz, 2H), 3.74 – 3.69 (m, 2H), 3.66 – 3.57 (m, 4H), 3.52 – 3.43 (m, 4H), 1.16 (t, J = 7.0 Hz, 3H). **^{13}C NMR (126 MHz, $CDCl_3$)** δ 164.00, 163.57, 140.64, 136.82, 132.67, 131.77, 130.91, 130.54, 130.11, 128.09, 127.75, 126.57, 126.25, 125.62, 121.31, 120.48, 119.30, 118.14, 70.79, 70.76, 70.31, 69.93, 68.00, 66.73, 39.27, 15.27. **HRMS (MALDI-TOF):** *m/z* calcd for $C_{26}H_{25}NNaO_5S$: 486.1349, found: 486.1346 (Δ = 0.58 ppm).

5-bromo-2-(2-(2-(2-ethoxyethoxy)ethoxy)ethyl)-1H-thioxantheno [2,1,9-def] isoquinoline-1,3(2H)-dione (*α*-BTI-Br): a solution of bromine at 1 M in DCM (0.474 mL, 0.474 mmol) was added, at room temperature, to **BTI-PE** (200 mg, 0.652 mmol) previously solubilized in dichloromethane (20 mL). The mixture was stirred for 4 h at room temperature before being poured into a saturated solution of $Na_2S_2O_4$. The aqueous phase was extracted with dichloromethane and the organic phase dried over $MgSO_4$ and concentrated under vacuum. The resulting solid was finally purified by column chromatography (eluent: DCM/EtOAc 7/3) to afford **α-BTI-Br** (230 mg, 98 % yield). **^{1}H NMR (300 MHz, $CDCl_3$)** δ 8.49 (d, J = 8.2 Hz, 1H), 8.46 (s, 1H), 8.13 – 8.06 (m, 2H), 7.44 – 7.38 (m, 3H), 4.39 (t, J = 6.1 Hz, 2H), 3.82 (t, J = 6.1 Hz, 2H), 3.74 – 3.69 (m, 2H), 3.67 – 3.57 (m, 4H), 3.53 – 3.43 (m, 4H), 1.16 (t, J = 7.0 Hz, 3H). **^{13}C NMR (76 MHz, $CDCl_3$)** δ 162.93, 162.78, 140.20, 135.87, 134.18, 131.90, 131.39, 130.24, 128.56, 128.09, 126.97, 126.75, 126.15, 125.71, 120.96, 119.64, 118.35, 114.35, 70.76, 70.25, 69.90, 67.93, 66.73, 39.37, 15.25. **HRMS (MALDI-TOF)**: *m/z* calcd for $C_{26}H_{24}NNaO_5SBr$: 564.04531, found: 564.0451 (Δ = 0.40 ppm).

2.3.3. Synthesis of α-BTI-PE

2-(2-(2-(2-ethoxyethoxy)ethoxy)ethyl)-5-(tetradec-1-yn-1-yl)-1H-thioxantheno [2,1,9-def] isoquinoline-1,3(2H)-dione (α-BTI-PE): degassed **α-BTI-Br** (100 mg, 0.184 mmol) and [$PdCl_2(PPh_3)_2$] (6.47 mg, 9.22 μmol) were dispersed in anhydrous and freshly distillated triethylamine (in a dry Schlenk tube) under inert atmosphere (5 mL). A dry solution of tetradec-1-yne (71.66 mg, 0.369 mmol) and copper(I) iodide (2.46 mg, 12.90 μmol) in anhydrous triethylamine (5 mL) was added dropwise at room temperature and under argon. Upon completion, the resulting mixture was heated at 60 °C overnight, still under inert atmosphere. Conversion was confirmed by TLC before pouring the reaction in water. The aqueous phase was treated with DCM and the organic phase was dried over $MgSO_4$ and concentrated. The resulting solid was purified by column chromatography (eluent: DCM) to afford **α-BTI-PE** as an orange-red powder (108 mg, 89 % yield). **^{1}H NMR (300 MHz, $CDCl_3$)** δ 8.61 (d, J = 8.2 Hz, 1H), 8.50 (s, 1H), 8.28 – 8.22 (m, 2H), 7.46 (ddt, J = 9.6, 6.1, 3.1 Hz, 3H), 4.43 (t, J = 6.1 Hz, 2H), 3.82 (t, J = 6.1 Hz, 2H), 3.74 – 3.69 (m, 2H), 3.66 – 3.57 (m, 4H), 3.52 – 3.43 (m, 4H), 2.62 (t, J = 7.0 Hz, 2H), 1.79 – 1.67 (m, 2H), 1.38 – 1.23 (m, 18H), 1.16 (t, 3H), 0.87 (t, J = 6.6 Hz, 3H). **^{13}C NMR (126 MHz, $CDCl_3$)** δ 163.71, 163.59, 136.68, 134.13, 132.31, 130.08, 127.86, 127.03, 126.10, 125.74, 121.26, 119.62, 117.61, 115.66, 102.21, 70.81, 70.76, 70.34, 69.94, 67.98, 66.73, 39.31, 32.07, 29.85, 29.82, 29.78, 29.52, 29.36, 29.16, 28.74, 22.83, 20.03, 15.27, 14.26. **HRMS (MALDI-TOF):** *m/z* calcd for $C_{40}H_{49}NNaO_5S$: 678.3225, found: 678.3224 (Δ = 0.56 ppm).

2.3.4. Synthesis of intermediates *p-BTA-Br* and *p-BTI-Br*

9-bromo-1H,3H-thioxantheno [2,1,9-def] isochromene-1,3-dione (*p*-BTA-Br): 6-bromonaphtalene anhydride (500 mg, 1.80 mmol) were placed in a microwave (20 mL) reactor followed by 2-amino-4-bromobenzenethiol (405 mg, 1.99 mmol), potassium carbonate (137 mg, 0.99 mmol) and finally, DMF (10 mL). This mixture was heated under microwave irradiation at 80 °C for 4 h. Then, amyl nitrite (727 mmL, 5.41 mmol) was added and a second round of heating was carried out but in conventional oil bath (80 °C overnight). The mixture was then cooled down and poured into 1 M HCl solution (100 mL). The solid that precipitated under these conditions was filtered off on a Büchner and successively washed with water, methanol, and ethanol to, in fine, afford ***p*-BTA-Br** (434 mg, 63 % yield) that was used without further purification. **^{1}H NMR (500 MHz, DMSO-d_6)** δ 8.65 (s, 1H), 8.58 (d, J = 7.9 Hz, 1H), 8.45 (d, J = 8.1 Hz, 1H), 8.31 (d, J = 8.0 Hz, 1H), 7.78 (d, J = 8.0 Hz, 1H), 7.71 (d, J = 8.9 Hz, 1H), 7.58 (d, J = 8.5 Hz, 1H). **HRMS (MALDI-TOF)**: *m/z* calcd for $C_{18}H_7O_3SBr$: 381.9300, found: 391.9294 (Δ = 1.64 ppm).

9-bromo-2-(2-(2-(2-ethoxyethoxy)ethoxy)ethyl)-1H-thioxantheno [2,1,9-def] isoquinoline-1,3(2H)-dione (*p*-BTI-Br): p-BTA-Br (250 mg, 0.652 mmol) was dissolved in 2-ethoxyethanol (20 mL) before adding 2-(2-(2-ethoxyethoxy)ethoxy)ethan-1-amine (127 mg, 0.718 mmol). After being refluxed overnight, the reaction mixture was poured into water (100 mL). The aqueous solution was extracted with dichloromethane and washed with brine. The resulting organic phase was dried over $MgSO_4$ before being evaporated under vacuum to afford a solid that was finally purified by column chromatography (eluent: DCM/EtOAc 7/3) to afford ***p*-BTI-Br** (76 % yield). **^{1}H NMR (300 MHz, $CDCl_3$)** δ 8.60 (d, J = 8.1 Hz, 1H), 8.41 (d, J = 8.0 Hz, 1H), 8.30 (d, J = 2.0 Hz, 1H), 8.11 (d, J = 8.3 Hz, 1H), 7.52 – 7.46 (m, 2H), 7.24 (d, J = 8.5 Hz, 1H), 4.43 (t, J = 6.1 Hz, 2H), 3.83 (t, J = 6.1 Hz, 2H), 3.74 – 3.69 (m, 2H), 3.65 – 3.58 (m, 4H), 3.52 – 3.45 (m, 4H), 1.17 (t, J = 7.0 Hz, 3H). **^{13}C NMR (76 MHz, $CDCl_3$)** δ 163.97, 163.54, 140.62, 136.77, 132.64, 131.74, 130.88, 130.49, 130.10, 128.03, 127.73, 126.54, 126.21, 125.55, 121.26, 120.45, 119.26, 118.10, 70.76, 70.30, 69.92, 67.99, 39.25, 15.26. **HRMS (MALDI-TOF):** *m/z* calcd for $C_{26}H_{24}NNaO_5SBr$: 564.0442, found: 564.0451 (Δ = −1.59 ppm).

2.3.5. Synthesis of *p-BTI-PE*

2-(2-(2-(2-ethoxyethoxy)ethoxy)ethyl)-9-(tetradec-1-yn-1-yl)-1H-thioxantheno [2,1,9-def] isoquinoline-1,3(2H)-dione (*p*-BTI-PE): Freshly distillated and anhydrous triethylamine (5 mL) was added to a blend of ***p*-BTI-Br** (100 mg, 0.184 mmol) and [$PdCl_2(PPh_3)_2$] (6.47 mg, 9.22 μmol) previously poured into a dry Schlenk tube under inert atmosphere (argon, vacuum-pump cycle on powders). In a separate flask was prepared a solution of tetradec-1-yne (71.66 mg, 0.369 mmol) and copper(I) iodide (2.46 mg, 12.90 μmol) in anhydrous trimethylamine (5 mL), also under inert atmosphere before being fully dropwise added to the BTI based solution at room temperature. The mixture was then heated under inert atmosphere at 60 °C and overnight. After completion (confirmed by TLC), the mixture was poured into water and extracted with DCM. The organic phase was washed with brine and concentrated under vacuum. The resulting solid was finally purified by column chromatography (eluent: DCM) to afford ***p*-BTI-PE** as an orange-red powder (107 mg, 88 % yield). **^{1}H NMR (300 MHz, $CDCl_3$)** δ 8.61 (d, J = 8.1 Hz, 1H), 8.41 (d, J = 8.0 Hz, 1H), 8.23 (d, J = 1.5 Hz, 1H), 8.19 (d, J = 8.3 Hz, 1H), 7.49 (d, J = 8.0 Hz, 1H), 7.39 (dd, J = 8.3, 1.5 Hz, 1H), 7.29 (d, J = 8.2 Hz, 1H), 4.44 (t, J = 6.2 Hz, 2H), 3.82 (t, J = 6.2 Hz, 2H), 3.74 – 3.68 (m, 2H), 3.66 – 3.57 (m, 4H), 3.53 – 3.43 (m, 4H), 2.45 (t, J = 7.1 Hz, 2H), 1.64 (q, J = 7.2 Hz, 2H), 1.48 (d, J = 8.0 Hz, 2H), 1.26 (s, 16H), 1.17 (t, J = 7.0 Hz, 3H), 0.90 – 0.85 (t, J = 6.6 Hz, 3H). **^{13}C NMR (126 MHz, $CDCl_3$)** δ 132.84, 132.75, 129.29, 126.42, 70.80, 70.33, 69.93, 68.00, 66.74, 29.83, 29.80, 29.69, 29.51, 29.32, 29.16, 28.79, 22.84, 19.64, 15.27, 14.27. **HRMS (MALDI-TOF)**: *m/z* calcd for $C_{40}H_{49}NNaO_5S$: 678.3225, found: 678.3224 (Δ = 0.16 ppm).

2.3.6. Synthesis of intermediates *m-BTA-Br* and *m-BTI-Br*

8-bromo-1H,3H-thioxantheno [2,1,9-def] isochromene-1,3-dione (*m*-BTA-Br): A microwave flask of 20 mL was charged with **6-bromonaphtalene anhydride** (1.10 g, 3.97 mmol), 2-amino-4-bromobenzenethiol (1.05 g, 5.16 mmol), potassium carbonate (329 mg, 2.38

mmol) and DMF (10 mL). This mixture was then irradiated by microwaves for 4 h at 80 °C. Amyl nitrite (1.60 mL, 11.91 mmol) was then added and the mixture was heated at 80 °C overnight with an oil bath. Once cooled down to room temperature, the mixture was poured into a 1 M HCl solution (100 mL). The precipitate was filtered on Büchner and washed with water, methanol, and ethanol. Once dried under vacuum, the resulting solid (***m*-BTA-Br**) was directly engaged in the next step without further purification (420 mg, 27 % yield). **^{1}H NMR (300 MHz, DMSO-d_6)** δ 8.63 (t, J = 7.5 Hz, 1H), 8.48 (d, J = 3.3 Hz, 1H), 8.38 (dd, J = 8.4, 2.9 Hz, 1H), 8.29 (dd, J = 8.0, 4.5 Hz, 1H), 7.94 (d, J = 2.1 Hz, 1H), 7.78 (d, J = 8.0 Hz, 1H), 7.65 (dd, J = 8.8, 2.1 Hz, 1H). **HRMS (EI-MS)**: *m/z* calcd for $C_{18}H_7O_3SBr$: 381.9299, found: 381.9303 (Δ = 0.50 ppm).

8-bromo-2-(2-(2-(2-ethoxyethoxy)ethoxy)ethyl)-1H-thioxantheno[2,1,9-def] isoquinoline-1,3(2H)-dione (*m*-BTI-Br): ***m*-BTA-Br** (100 mg, 0.261 mmol) and 2-(2-(2-ethoxyethoxy)ethoxy)ethan-1-amine (92.5 mg, 0.522 mmol) were combined in ethanol (15 mL) and refluxed overnight under inert atmosphere. The reaction mixture was then diluted with dichloromethane and the organic phase was washed with water and brine before being dried over $MgSO_4$. After evaporation of the solvent, the crude was purified by column chromatography on silica gel using CH_2Cl_2 as eluent affording the corresponding compound ***m*-BTI-Br** (80 mg, 56 % yield). **^{1}H NMR (300 MHz, $CDCl_3$)** δ 8.54 (d, J = 8.1 Hz, 1H), 8.38 (d, J = 8.0 Hz, 1H), 8.08 (d, J = 8.2 Hz, 1H), 7.98 (d, J = 8.6 Hz, 1H), 7.51 – 7.40 (m, 3H), 4.42 (t, J = 6.1 Hz, 2H), 3.82 (t, J = 6.1 Hz, 2H), 3.74 – 3.67 (m, 2H), 3.66 – 3.55 (m, 4H), 3.53 – 3.42 (m, 4H), 1.16 (t, J = 7.0 Hz, 3H). **^{13}C NMR (75 MHz, $CDCl_3$)** δ 163.84, 163.43, 139.48, 135.97, 133.65, 132.63, 131.02, 130.88, 130.45, 128.81, 127.55, 127.11, 125.44, 124.55, 121.65, 120.66, 119.36, 118.56, 70.76, 70.27, 69.92, 67.97, 66.74, 39.29, 15.27. **HRMS (MALDI-TOF)**: *m/z* calcd for $C_{26}H_{24}NNaO_5S$: 564.0445, found: 564.0451 (Δ = −1.07 ppm).

2.3.7. Synthesis of *m*-BTI-PE

2-(2-(2-(2-ethoxyethoxy)ethoxy)ethyl)-8-(tetradec-1-yn-1-yl)-1H-thioxantheno[2,1,9-def] isoquinoline-1,3(2H)-dione (*m*-BTI-PE): To an oven dried Schlenk tube filled with argon, compound ***m*-BTI-Br** (80 mg, 0.147 mmol), CuI (2 mg, 0.010 mmol) and [$PdCl_2$ (PPh_3)$_2$] (10 mg, 0.014 mmol) were sequentially added. After addition of freshly distilled and degassed NEt_3 (5 mL), then tetradec-1-yne (57 mg, 0.295 mmol, 2 eq) the reaction mixture was heated at 90 °C for 48 h under inert atmosphere. Conversion of the starting material was followed by TLC before cooling down the reaction mixture and pouring the latter in water. This aqueous phase was extracted with DCM, then the combined organic phases were washed with brine before, dried over $MgSO_4$ and concentrated under vacuum. The resulting solid was finally purified by column chromatography (eluent: DCM) to afford ***m*-BTI-PE** as an orange-red powder (55 mg, 60 %). **^{1}H NMR (300 MHz, $CDCl_3$)** δ 8.59 (d, J = 8.1 Hz, 1H), 8.40 (d, J = 7.9 Hz, 1H), 8.12 (dd, J = 11.8, 8.4 Hz, 2H), 7.48 (d, J = 8.0 Hz, 1H), 7.42 – 7.33 (m, 2H), 4.43 (t, J = 6.2 Hz, 2H), 3.82 (t, J = 6.1 Hz, 2H), 3.76 – 3.67 (m, 2H), 3.67 – 3.55 (m, 4H), 3.54 – 3.40 (m, 4H), 2.44 (t, J = 7.0 Hz, 2H), 1.58 (s, 2H), 1.52 – 1.38 (m, 2H), 1.34 – 1.24 (m, 16H), 1.16 (t, J = 7.0, 0.8 Hz, 3H), 0.92 – 0.82 (m, 3H). **^{13}C NMR (75 MHz, $CDCl_3$)** δ 164.00, 163.57, 140.41, 136.49, 132.70, 131.80, 130.98, 130.71, 129.08, 127.03, 126.33, 125.99, 125.57, 121.28, 120.57, 119.46, 118.21, 94.97, 70.75, 70.24, 69.92, 67.96, 66.74, 32.07, 29.81, 29.68, 29.52, 29.29, 29.10, 28.65, 22.85, 19.70, 15.28, 14.30. **HRMS (MALDI-TOF):** *m/z* calcd for $C_{40}H_{49}NNaO_5S$: 678.3220, found: 678.3224 (Δ = −0.54 ppm).

2.4. Spectrophotometric and spectrofluorimetric measurements

2.4.1. Photophysical characterization and titrations

Photophysical characterizations were performed by preparation of stock solutions of ***p*-BTI-PE, *α*-BTI-PE, *m*-BTI-PE, BTI-C6, BTI-C12** and **BTI-C16** (*ca.* 10^{-3} M) in $CHCl_3$, and THF, by dissolution of an appropriate amount of the selected compound in a 10 mL volumetric flask. Further studies were carried out by appropriate dilution of the stock solutions up to 10^{-5} – 10^{-6} M.

Luminescence spectra of the compounds in the solid state and of doped polymer thin films were recorded using of a fiber-optics device connected to the spectrofluorometer while exciting the samples at appropriated wavelength. The temperature dependent emission spectra were recorded by heating the samples over a hotplate with control over the temperature.

2.4.2. Fluorescence quantum yield and lifetime

Relative photoluminescence quantum yields were measured using the ultrabright benzothioxanthene imide in dichloromethane as a standard solution (ϕ_F = 0.99) for quantifying the relative QY of all compounds dissolved in the THF and chloroform [24]. Tempro Fluorescence Lifetime System with a Nanoled pulsed diode controller from Horiba Jobin-Yvon (PROTEOMASS Scientific Society Facilities) was used to perform lifetime measurements.

2.5. Preparation of polymer Dye-Doped thin films

Polymethylmethacrylate (PMMA), and Kurarity doped polymer thin films were obtained by slow evaporation of a 10 mL chloroform solution containing 100 mg of the corresponding polymer matrix, and 0.5 mg of the selected compound. All mixtures were poured onto PFA supports with diameter of 5 cm to allow solvent evaporation at room temperature.

3. Results and discussion

3.1. Synthesis

The synthetic routes to the six derivatives designed and considered herein are depicted in Scheme 1.

Imidization of **BTA** was carried out in ethoxyethanol by reacting with the corresponding amine to afford the aliphatic side chain functionalized **BTI-C6**, **BTI-C12**, **BTI-C16,** as well as the polyether derivative **BTI-PE** that was subsequently brominated with bromine and finally engaged in a Sonogashira cross coupling reaction yielding the **α-BTI-PE** derivative. Its regioisomers, *i.e.* ***p*-BTI-PE** and ***m*-BTI-PE**, were prepared from a common strategy consisting in reacting the corresponding bromoaminothiophenol (2-amino-4-bromobenzenethiol or 2-amino-5-bromothiophenol, respectively) with the commercially available 6-bromo-1H-benzo[de]isoquinoline-1,3(2H)-dione. Ring was closed by Pschorr reaction in presence of amyl nitrite, the resulting anhydrides ***m*-BTA-Br** and ***p*-BTA-Br** were imidized and finally engaged in a similar palladium-catalyzed cross coupling reaction than **α-BTI-PE** to afford the structural isomers ***m*-BTI-PE** and ***p*-BTI-PE,** respectively.

The molecular structures of compounds **BTI-C6** and **BTI-C16** were further confirmed by means of single-crystal X-ray diffraction analysis. Their molecular structures are depicted in Fig. 2, while selected bond distances and angles are presented in Table 2.

Both compounds crystallized in the triclinic system, *P*-1 space group, with a single molecule in the asymmetric unit. As expected, both compounds show similar features, with the BTI moieties displaying planar backbones, which can be perfectly superimposed when both structures are overlayed (Figure S1). However, different 3D arrangements are shown for the aliphatic side chains of six and sixteen carbon atoms, for **BTI-C6** and **BTI-C16**, respectively. All bond distances and angles are within the expected values for similar compounds [30]. The supramolecular arrangement observed in **BTI-C6** is generated from the establishment of non-classical hydrogen bonds of the type C–H…O (Figure S2 and Table S1) and of π…π interactions, that lead to the formation of dimers with an inverted BTI core in a head-to-tail a pattern. A similar 3D arrangement is observed for **BTI-C16** (Figure S3 and Table S1).

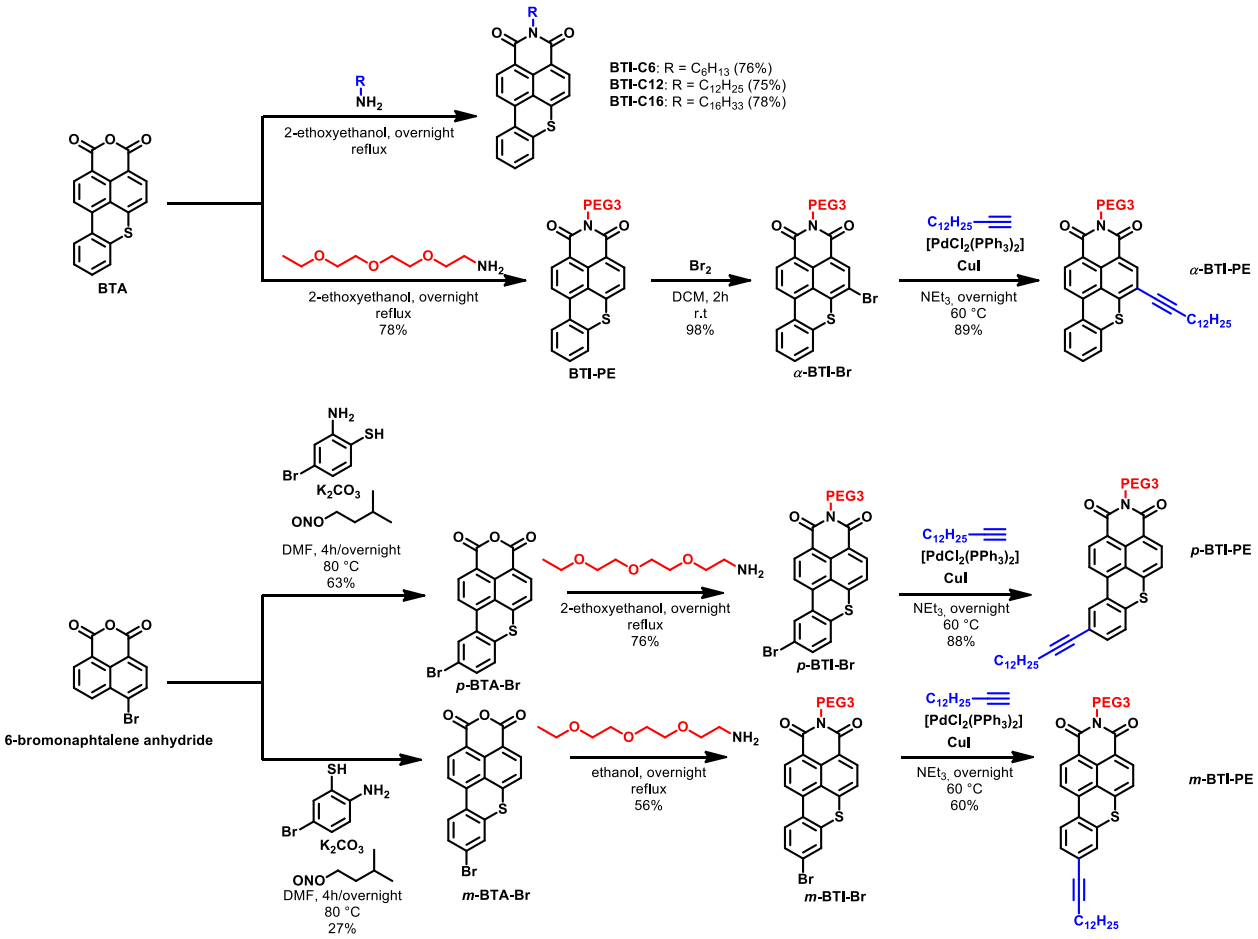

Scheme 1. Synthetic route to **BTI-C6**, **BTI-C12**, **BTI-C16**, ***m*-BTI-PE**, ***p*-BTI-PE** and **α-BTI-PE.**

3.2. Mesomorphic behavior

The liquid crystal properties of the new compounds were studied by polarized light optical microscopy (POM), differential scanning calorimetry (DSC) and powder X-ray diffraction (PXRD). Table 3 summarizes the thermal behavior of all compounds, gathering the onset temperature of the phase transitions and the corresponding enthalpy data calculated by DSC.

POM observations reveal that compounds ***p*-BTI-PE** and ***m*-BTI-PE** behave as enantiotropic liquid crystals and form SmA mesophases in both heating and cooling processes. Although the texture of ***p*-BTI-PE** is not well-defined (Fig. 3a), the growth of bâtonnet structures in ***m*-BTI-PE** during its isotrope-mesophase phase transition could be captured (Fig. 3b). A moment later, at the same temperature, all bâtonnet structures merged to form the typical fan-shaped texture created when molecules are fully self-assembled in the SmA mesophase (Fig. 3c, Video S1) [31,32]. The analysis of the DSC thermograms confirms the phase behavior found for these species (see Figures S4-S9). In particular, the melting process was not observed for ***p*-BTI-PE**, and only a unique endothermic peak appears at 76 °C when the SmA mesophase transforms into the isotropic liquid. For ***m*-BTI-PE**, three endothermic peaks were monitored at 51, 66 and 137 °C, attributed to the solid–solid, solid-mesophase and mesophase-isotrope phase transitions, respectively. Although the melting process was detected in the latter case, this molecular reorganization was found to require a low amount of energy (enthalpy value of *ca.* 4.0 kJ/mol). Upon cooling, the exothermic peak attributed to the isotrope-mesophase phase transitions was well-detected for both compounds, whereas the solidification process was solely observed in the DSC trace of ***p*-BTI-PE**, most likely due to a glass formation or a partial crystallization of ***m*-BTI-PE** from the mesophase. In fact, the solid–solid phase transitions were not observed in successive heating/cooling cycles.

On the other hand, compounds **BTI-C12** and **BTI-C16**, functionalized with a terminal alkyl chain, also exhibit mesomorphism, giving rise to fan-shaped textures of a SmA mesophase upon cooling (Fig. 3d,e). Focal-conic textures were also observed in small domains (drops of isotropic liquid) because of the grown of the mesophase from the isotropic liquid in confined regions (Fig. 3f). The DSC traces are consistent with the POM observations and show the corresponding endothermic and exothermic peaks for each phase transition, except for the melting process in **BTI-C12**, which was not detected (Figure S8). Additional endothermic peaks were also monitored before the melting temperature, for both compounds, resulting from transformations in the solid state. Note that the corresponding solid–solid phase transitions observed on heating were not detected upon cooling or subsequent heating/cooling cycles, which could be again associated with a glass formation from the SmA mesophase on cooling.

To confirm the lamellar arrangement of molecules in the liquid-crystalline phase, temperature-dependent X-ray diffraction studies were performed for compounds ***m*-BTI-PE** and **BTI-C16**, which were selected as representative examples of both families of compounds. As observed in Fig. 4, the diffractogram registered for ***m*-BTI-PE** at 80 °C displays a series of four peaks with a reciprocal d-spacing ratio of 1:1/2:1/3:1/4 corresponding to the (001), (002), (003) and (004) reflections of a lamellar lattice (lamellar periodicity, d = 30.5 Å). In addition, a broad diffuse halo was also observed at around 4.7 Å, a clear indication of the liquid-like order of the molten alkyl chains in the mesophase [33]. Interestingly, diffractograms obtained before the

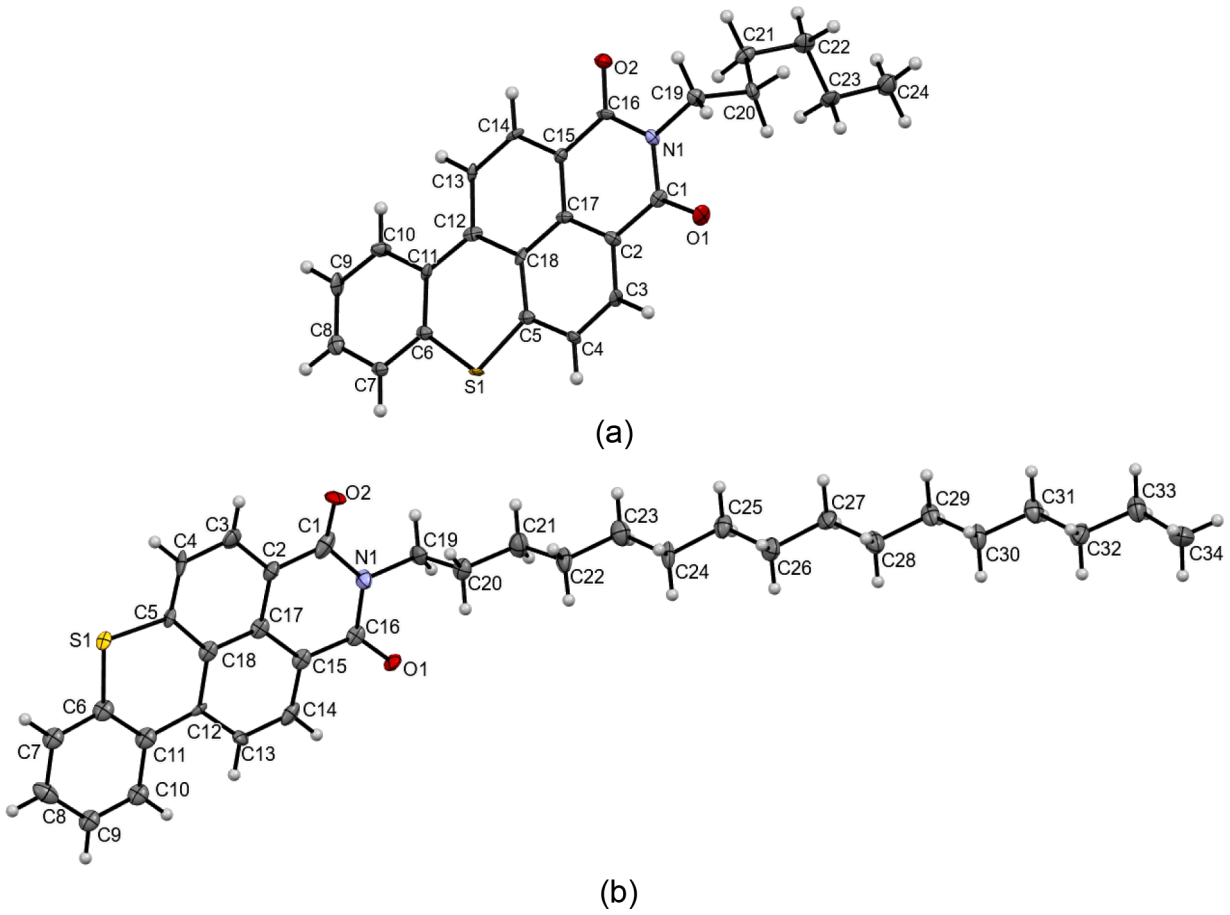

Fig. 2. Mercury representation of the molecular structure of compounds (a) **BTI-C6** and (b) **BTI-C16**.

Table 2
Selected bond lengths (Å) and angles (°) for **BTI-C6** and (b) **BTI-C16**.

	BTI-C6	BTI-C16
Bond lengths		
C1–N1	1.416(8)	1.381(13)
C1–O1	1.218(7)	1.201(15)
C16–N1	1.393(8)	1.408(14)
C16–O2	1.227(7)	1.219(11)
C19–N1	1.471(8)	1.482(14)
C5–S1	1.749(6)	1.753(10)
C6–S1	1.759(6)	1.750(12)
Bond angles		
C1–N1–C16	123.5(5)	125.4(10)
N1–C1–O1	119.5(6)	121.3(11)
N1–C16–O2	119.7(5)	120.6(10)
C5–S1–C6	103.4(3)	103.5(5)

Table 3
Thermal and phase behavior established by DSC.

Compound	Transitions[a]	T[b] [°C] (ΔH [kJ/mol])
***p*-BTI-PE**	Cr → SmA → I	58[c], 76 (40.6)
	I → SmA → Cr	65 (−5.3), 59 (−1.7)
α-BTI-PE	Cr → I	90 (43.1)
	I → Cr	50 (−21.0)
***m*-BTI-PE**	Cr → Cr' → SmA → I	51 (35.2), 66 (4.0), 137 (15.6)
	I → SmA → Cr	132 (−17.7), 45[c]
BTI-C6	Cr → I	150 (20.1)
	I → Cr	95 (−8.9)
BTI-C12	Cr → Cr' → SmA → I	39 (14.8), 83[c], 120 (21.4)
	I → SmA → Cr	91 (−1.0), 67 (−10.8)
BTI-C16	Cr → Cr' → Cr'' → SmA → I	36 (5.0), 51 (0.8), 106 (0.2), 114 (27.1)
	I → SmA → Cr	106 (−1.9), 87 (−13.8)

[a] Cr, Cr', Cr'' = solid phase, SmA = Smectic A mesophase, I = isotropic liquid.
[b] DSC onset peaks.
[c] Determined by POM.

melting temperature show that the initial solid phase of ***m*-BTI-PE** evolves in another solid one, at 51 °C, in which molecules start to self-assemble in a lamellar arrangement (Figure S10). This process eases the formation of the mesophase in terms of energy since the same supramolecular ordering is maintained in both the new solid and the mesophase. This feature is in consistency with the low enthalpy value associated to the solid-mesophase phase transition compared to those calculated for the solid–solid and the mesophase-liquid ones (see Table 3).

By contrast, no diffraction peaks were recorded in the mesophase of **BTI-C16**, except for the typical broad halo at *ca.* 4.6 Å attributed to the liquid-like order of the alkyl chains. The origin of this feature could be attributed to the formation of a SmA mesophase with a high degree of disorder. Nonetheless, when the mesophase transforms into the solid phase, three sharp diffraction peaks with a reciprocal d-spacing ratio of 1:1/2:1/3 appeared in the low-angle region. Most likely, the self-assembly of molecules in the SmA mesophase is maintained during the solidification process, thus confirming the lamellar nature of the liquid-crystalline phase.

Interestingly, rationalization of these results clearly highlights that the position of the alkyl chain in compounds ***p*-BTI-PE**, **α-BTI-PE** and ***m*-BTI-PE** plays a crucial role in the mesomorphism induction. While molecules of ***p*-BTI-PE** and ***m*-BTI-PE** are capable to self-assembled into SmA mesophases, the lateral alkyl chain of **α-BTI-PE** was found to hinder the assembly in a lamellar arrangement. Likewise, the chain

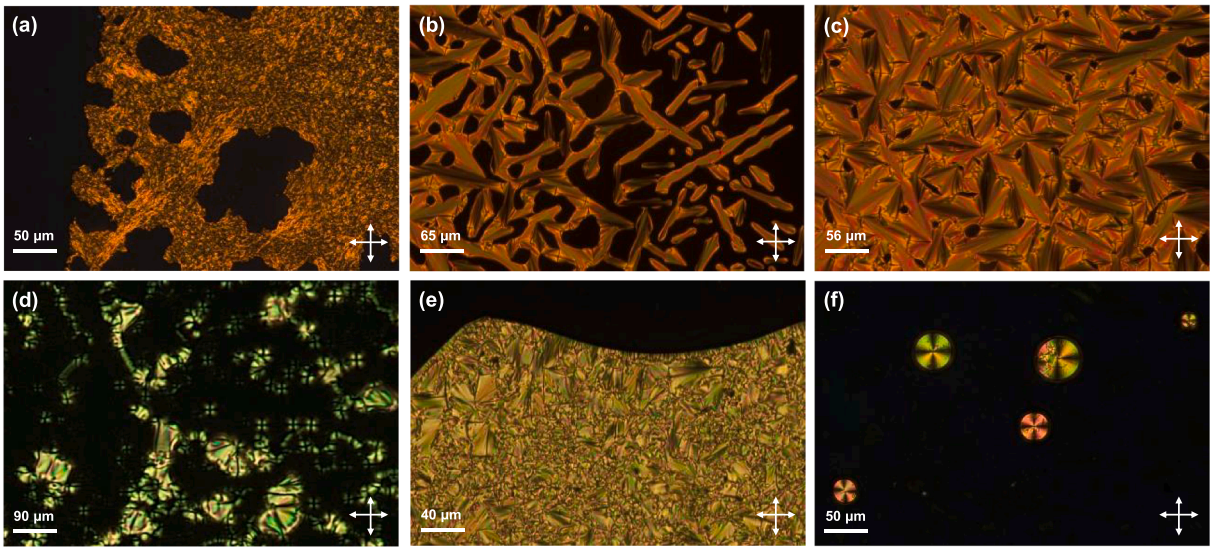

Fig. 3. POM microphotographs showing the SmA mesophases for compounds (a) ***p*-BTI-PE** at 59 °C, (b,c) ***m*-BTI-PE** at 132 °C, (d) **BTI-C12** at 91 °C, and (e,f) **BTI-C16** at 105 °C. All images were taken with crossing polarizers upon cooling. Scale bar is also included.

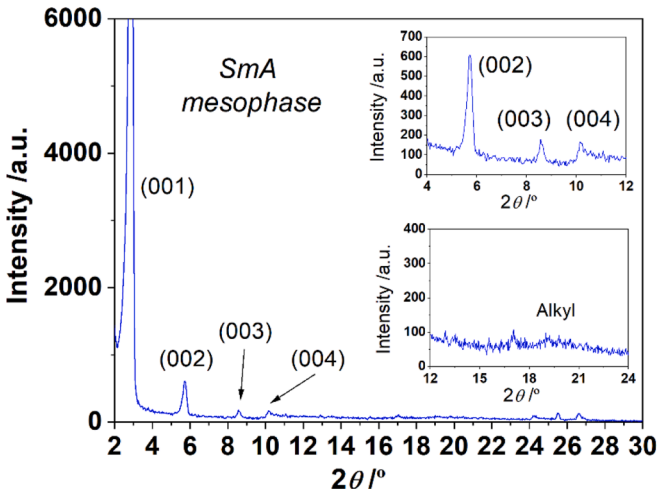

Fig. 4. X-ray diffractogram registered in the SmA mesophase of ***m*-BTI-PE** at 80 °C upon heating.

length can also be a key factor, as observed in compounds **BTI-C6**, **BTI-C12** and **BTI-C16**, to achieve liquid crystal properties.

3.3. Photophysical characterization

The ultrabright benzothioxanthene imide derived compounds exhibit luminescence properties both in solution and in the solid state. All six compounds can be easily grouped into two families with the predisposed intention to understand how i) the incorporation of different types of side chains, *i.e.*, either alkyl or both alkyl and PEG, ii) different lengths in carbon atoms number, and iii) position on the benzothioxanthene imide core might be impactful on their photophysical and liquid crystal properties. In this context, Fig. 5 displays the photophysical data collected at 298 K for compounds ***m*-BTI-PE** and **BTI-C16** in THF and chloroform as a representative example (Figure S11), while Table 4 gathers all the photophysical data of the studied compounds. Overall, the UV–Vis spectra show a band centered at 452 and 457 nm for the two classes of compounds in THF that manifest a slight redshift when studies were carried out in chloroform. This band is associated with the π-π* transition of the benzothioxanthene imide chromophore, contributing to the visualization of green-yellowish solutions in the naked eye.

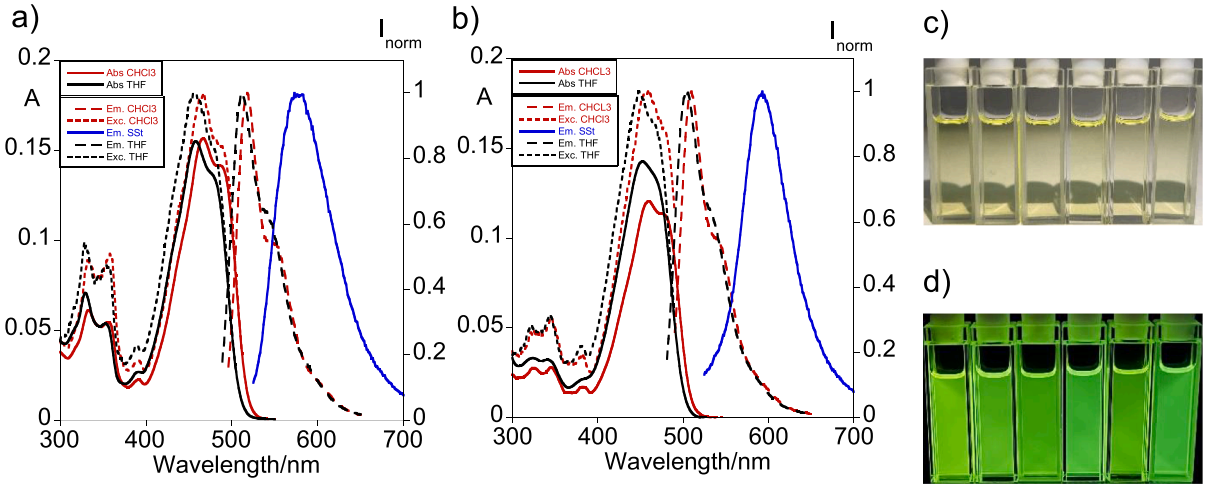

Fig. 5. Photophysical characterization of derivatives (a) ***m*-BTI-PE**, and (b) **BTI-C16** in chloroform and THF ([***m*-BTI-PE**] = [**BTI-C16**] = 5 μM). Images follow the order ***m*-BTI-PE**, **α-BTI-PE**, and ***p*-BTI-PE** in chloroform and THF (c) under natural light and (d) irradiated at 365 nm.

Table 4
Absorption maximum wavelength in solution (λ_{abs}), emission maximum wavelength in solution (λ_{em}), molar absorption coefficients (ε), Stokes shift (Δ λ), emission maximum in the solid state (λ_{em}^{Solid}), fluorescence quantum yields (ϕ), fluorescence lifetimes (τ) for compounds ***p*-BTI-PE**, **α-BTI-PE**, ***m*-BTI-PE**, **BTI-C6**, **BTI-C12** and **BTI-C16** in THF and chloroform.

Cpd.	Solv.	λ_{abs} [nm]	λ_{em} [nm]	ε [10^4 cm^{-1} M^{-1}]	Stokes shift [cm^{-1}]	λ_{em}^{Solid} [nm]	ϕ	τ [ns]
***p*-BTI-PE**	THF	457	512	27,026	2350.6	577	0.88	6.6
	$CHCl_3$	466	518	24,770	2154.2		0.92	6.8
α-BTI-PE	THF	457	511	20,733	2312.4	591	0.93	8.1
	$CHCl_3$	466	520	23,065	2228.5		0.91	8.2
***m*-BTI-PE**	THF	458	512	27,896	2302.8	573	0.85	6.1
	$CHCl_3$	466	517	29,597	2116.9		0.89	6.4
BTI-C6	THF	452	505	29,592	2321.9	582	0.94	7.2
	$CHCl_3$	461	510	21,450	2084.1		0.99	6.9
BTI-C12	THF	452	505	28,771	2321.9	588	0.93	7.2
	$CHCl_3$	461	510	23,715	2084.1		0.99	6.9
BTI-C16	THF	452	505	28,584	2321.9	593	0.94	7.2
	$CHCl_3$	461	510	23,032	2084.1		0.99	6.9

Upon excitation at the appropriate wavelength, the samples emit a green light with a maximum between 505 and 512 nm in THF while emission in the 510 and 520 nm range is observed in chloroform resulting in a stoke shift ranging from 2084 to 2350 cm^{-1} for all compounds. On a relatable note, solid-state emission spectra (Fig. 5a-b; Em. SSt spectra in blue) display a more pronounced variability and a significant shift regarding the emission in solution due to the influence of the different chains on the self-assembling properties. Interestingly, whereas a small variation, from 577 to 573 nm, was monitored for ***p*-BTI-PE** and ***m*-BTI-PE**, respectively, related to the introduction of the alkyl chain in adjacent carbon atoms of the lower benzene ring, a more pronounce shift to 591 nm was observed for **α-BTI-PE**, in which the same alkyl chain was selectively introduced on the upper naphthyl ring, in alpha of the sulfur atom. Regarding **BTI-C6**, **BTI-C12** and **BTI-C16**, it is noteworthy that increasing the length of alkyl chain functionalizing the imide moieties resulted in a progressive bathochromic shift.

From a quantum yield perspective, near-unity photoluminescence was estimated for almost all compounds maintaining, in consistency with the early reported data on BTI,[24] except for ***m*-BTI-PE** that was characterized by a quantum yield below 90 %.

Single digit nanosecond times were achieved for life-time measurements in all compounds with minor variations for ***p*-BTI-PE**, **α-BTI-PE** and ***m*-BTI-PE**, once again potentially related to the different grafting position of the alkyl chain on the π-conjugated core.

3.4. Polymer supported temperature dependent studies

Since *i*) all compounds demonstrated emission in the solid state and *ii*) ***m*-BTI-PE** and **BTI-C16** display the best mesophase temperature ranges, our next intention was to understand how this behavior affects the emission alongside the incorporation into solid supported materials while exposed to temperature increases. Starting with recorded on their powder form (Fig. 6 and S12), it turned out that a linear relation between emission and temperature from 40 to 100 °C was monitored for **BTI-C16** whereas, in stark contrast, no such behavior was observed for ***m*-BTI-PE**. Overall, the increase of temperature causes a hypsochromic shift and a broadening of the emission band with emission maximum centered at 555 and 565 nm for ***m*-BTI-PE** and **BTI-C16**, respectively. After the cooling process, a return to the initial emissions maximum wavelength was observed. However, only a recovery of around 50 % was reached most likely due to the changes in positioning of the molecules due to the phase transition.

In consistency with the previous findings, PMMA and Kurarity thin films doped with either ***m*-BTI-PE** or **BTI-C16** have been processed and investigated to rationalize the evolution of thermally dependent emission in solid supported matrixes. Fig. 7a-d gathers the emission profile of a warming (until 120 °C) and cooling cycle (back to room temperature) while Fig. 6e gathers the images of the studied materials. Overall, a clear change in the emission wavelength of all polymers doped thin films were recorded within the 505 to 515 nm range, in agreement with those monitored in solution. Giving our focus to the PMMA films, two distinct

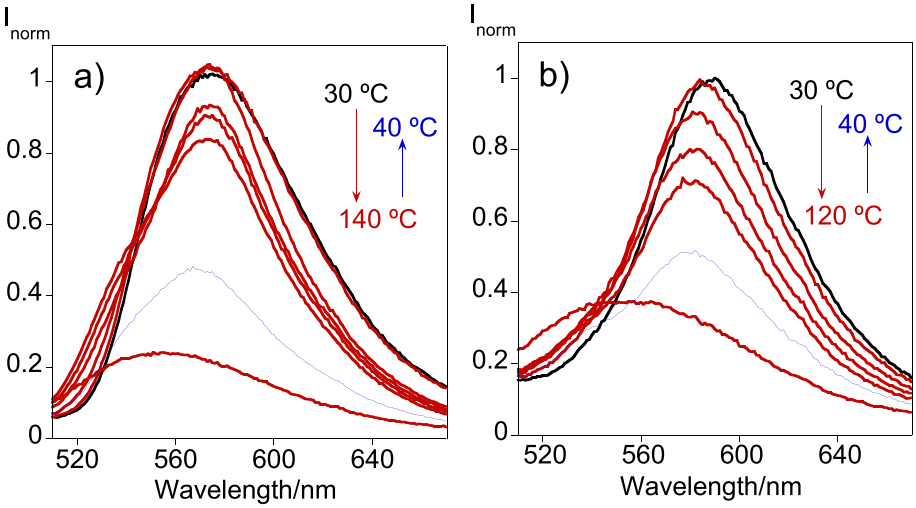

Fig. 6. Temperature-dependent emission spectra of (a) ***m*-BTI-PE** and (b) **BTI-C16** in the solid state collected through a warming and cooling cycle. For clarity of the reader the black spectrum represents the initial emission at 30 °C, the red arrow suggests the progression with increase in temperature and the blue spectrum is recorded back at 40 °C. (For interpretation of the references to color in this figure legend, the reader is referred to the web version of this article.)

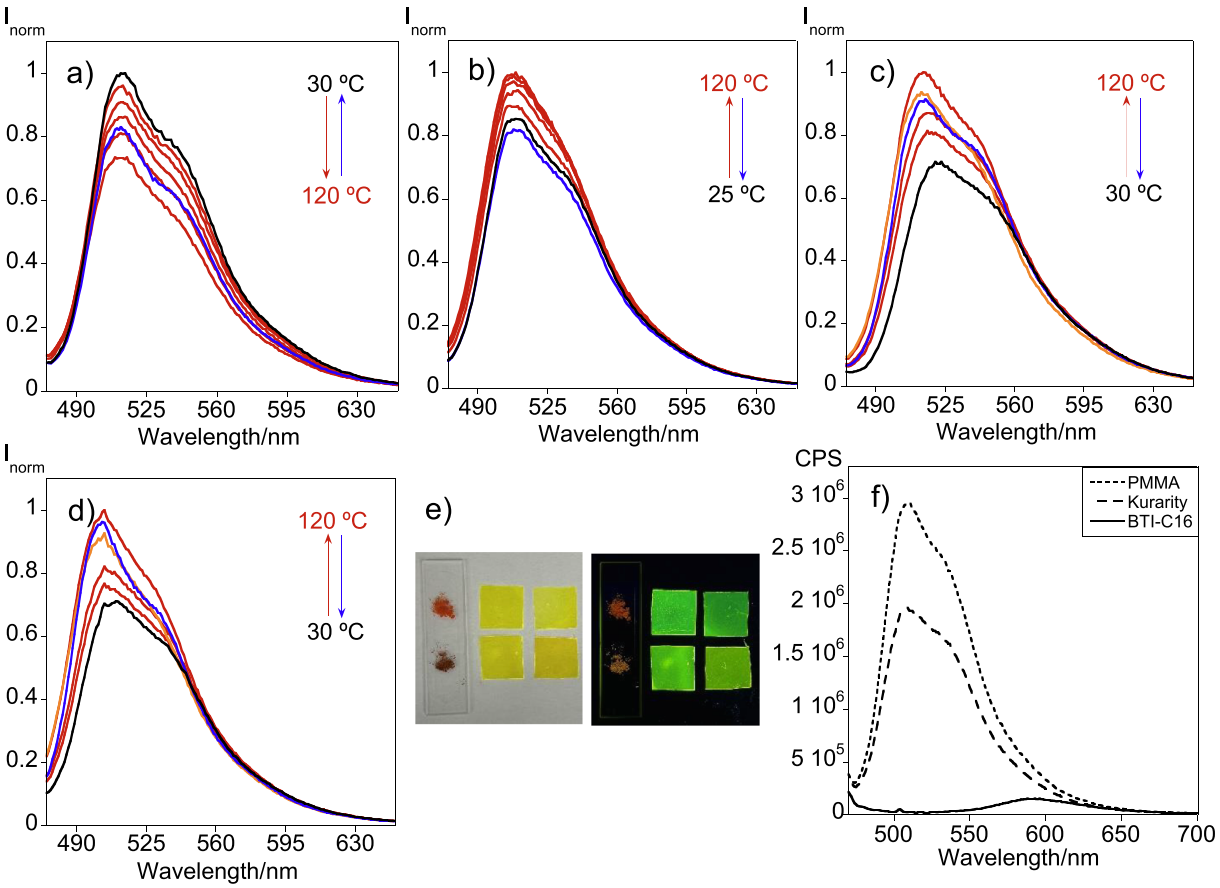

Fig. 7. Temperature-dependent emission spectra of PMMA doped with (a) ***m*-BTI-PE** and (b) **BTI-C16** and Kurarity films doped with (c) ***m*-BTI-PE** and (d) **BTI-C16** collected through a warming and cooling cycle. For clarity of the reader the black spectrum represents the initial emission at 30 °C, the red arrow suggests the progression with increase in temperature and the blue spectrum is recorded back at 30 °C. For Kurarity polymers the spectra noted in orange represents the emission recorded at 120 °C. (e) Images under natural light (left) and under UV irradiation (right) of **BTI-C16** (upper line) and ***m*-BTI-PE** (lower line) in powder form, doped in PMMA and Kurarity, respectively. (f) Emission spectra in counts per second of PMMA and Kurarity polymers doped with **BTI-C12** and the respective spectrum in solid state for comparison taken at 25 °C. (For interpretation of the references to color in this figure legend, the reader is referred to the web version of this article.)

behaviors can be perceived. First, in the case of ***m*-BTI-PE** doped films (Fig. 7a), a quenching of the emission was observed until 120 °C with a slight recovery on the emission after cooling. On the other hand, the opposite was found for **BTI-C16** doped film (Fig. 7b) since a clear increase in emission, of around 20 %, along the rise of temperature was observed. Although these findings are not a linearly correlated to the temperature, and for this reason cannot be used as molecular thermometers, such increase in emission have already been reported with other polymer matrix doped with alkyl chains containing chromophores [34]. This can be attributed to the increase in rigidity of the polymer upon heating in addition to increased thermal dissipation from the polymer which in turn prevents the chromophore from opting for non-radiative relaxation pathways. At the end of the cooling stage the emission returns to initial one.

Regarding Kurarity doped films (Fig. 7c-d), the same behavior was found for both films where a clear increase of *ca.* 30 % in the emission was observed at 100 °C followed by a slight decrease when temperatures reached 120 °C. Upon cooling, the polymers' emission did not suffer any relevant changes maintaining the overall increase in emission during the process.

As means of comparison, Fig. 7f shows the intensities of the materials studied for **BTI-C16**. Giving a special attention to the intensities, it is possible to perceive that both doped materials exceed by far the emission of their respective powder form. Taking into consideration that all spectra have been recorded at 25 °C with a slit aperture of 1.5 nm, the doped materials indeed exhibit a significant increase of *ca.* 19 and 13 times the emission observed in solid state for PMMA and Kurarity polymers respectively. Thus, these materials have shown significant relevance for applications that might require to maintain the emission properties with temperature variations.

4. Conclusion

In conclusion, a series of benzothioxanthene imide derivatives specifically designed towards the pioneer evaluation of potential liquid crystal properties have been synthesized and fully characterized. Polarized light optical microscopy (POM), differential scanning calorimetry (DSC), powder X-ray diffraction (XRD) and photophysical studies have been carried out. Mesomorphic studies of these compounds suggest the relevance of the position of the alkyl chain in compounds ***p*-BTI-PE**, **α-BTI-PE** and ***m*-BTI-PE** for the induction of LC properties. While rod-like molecules of ***p*-BTI-PE** and ***m*-BTI-PE** were observed to self-assembled into SmA mesophases, **α-BTI-PE** had its mesomorphism impaired due to the lateral alkyl chain. Equally, the chain length has been found as an important factor, as observed in compounds **BTI-C6**, **BTI-C12** and **BTI-C16**, to achieve liquid crystal properties. Photoluminescent studies point out the consistency from early reported BTI data to manifest near-unity quantum yields, a key parameter when considering dyes' applications. Temperature dependent studies demonstrated a hypsochromic shift and a broadening of the emission band with its quenching for ***m*-BTI-PE** and **BTI-C16** in powder form. Solid state studies have been extended towards incorporation of these

dyes in polymeric matrixes that provided the enhanced emission and robustness regarding temperature stability, opening new avenues for the use of BTI derivatives.

Funding

This work received support and help from FCT/MCTES (LA/P/0008/2020 DOI https://doi.org/10.54499/LA/P/0008/2020, UIDP/50006/2020 DOI https://doi.org/10.54499/UIDP/50006/2020 and UIDB/50006/2020 DOI https://doi.org/10.54499/UIDB/50006/2020), through national funds. PROTEOMASS Scientific Society (Portugal) is acknowledged by the funding provided through the General Funding Grant 2023–2024, and by the funding provided to the Laboratory for Biological Mass Spectrometry Isabel Moura (#PM001/2019 and #PM003/2016). This research was also supported by Complutense University of Madrid (GRFN32/23 and PR3/23–30828).

CRediT authorship contribution statement

Frederico Duarte: Writing – review & editing, Writing – original draft, Software, Methodology, Investigation, Funding acquisition, Formal analysis, Data curation. **Korentin Morice:** Writing – original draft, Validation, Software, Investigation, Formal analysis, Data curation. **Tatiana Ghanem:** Software, Methodology, Investigation, Formal analysis, Data curation. **Darío Puchán Sánchez:** Writing – review & editing, Software, Methodology, Investigation, Formal analysis, Data curation. **Philippe Blanchard:** Writing – review & editing, Validation, Supervision, Methodology, Funding acquisition, Formal analysis, Data curation. **Clara S. B. Gomes:** Writing – review & editing, Validation, Software, Investigation, Formal analysis, Data curation. **Santiago Herrero:** Writing – review & editing, Funding acquisition, Data curation. **Clement Cabanetos:** Writing – review & editing, Writing – original draft, Supervision, Resources, Methodology, Funding acquisition, Formal analysis, Data curation, Conceptualization. **Cristián Cuerva:** Writing – review & editing, Writing – original draft, Validation, Supervision, Methodology, Investigation, Funding acquisition, Formal analysis, Data curation. **Jose Luis Capelo-Martinez:** Writing – review & editing, Visualization, Validation, Resources, Funding acquisition. **Carlos Lodeiro:** Writing – review & editing, Validation, Supervision, Resources, Project administration, Methodology, Funding acquisition, Formal analysis, Data curation, Conceptualization.

Declaration of competing interest

The authors declare the following financial interests/personal relationships which may be considered as potential competing interests: [Carlos Lodeiro reports financial support was provided by Proteomass Scientific Society. If there are other authors, they declare that they have no known competing financial interests or personal relationships that could have appeared to influence the work reported in this paper.].

Data availability

Data will be made available on request.

Acknowledgements

F.D. thanks to FCT/MCTES (Portugal) for his doctoral grant 2021.05161.BD. French National Research Agency ‘ANR’ for the project BTXI-Apogee ref: ANR-20-CE05-0029). D.P.S and K.M. acknowledge the MITI of the CNRS and the ANR (BTXI-Apogee, ANR-20-CE05-0029) for their PhD grants respectively. C. S. B. Gomes acknowledges the XTAL – Macromolecular Crystallography group (UCIBIO and i4HB) for granting access to the X-ray diffractometer. X-Ray infrastructure financed by FCT-MCTES through project RECI/BBBBEP/0124/2012.

Appendix A. Supplementary material

Supplementary data to this article can be found online at https://doi.org/10.1016/j.molliq.2024.125424.

References

[1] G. Singh, S.-W. Kang, S. Kumar, Structures: liquid crystals, Encyclop. Condens. Matter Phys. 5 (2024) 375–389, https://doi.org/10.1016/B978-0-323-90800-9.00244-4.
[2] A. Kumar, G. Singh, Recent advances and future perspectives of photoluminescent liquid crystals and their nanocomposites for emissive displays and other tunable photonic devices, J. Mol. Liq. 386 (2023) 122607, https://doi.org/10.1016/j.molliq.2023.122607.
[3] M. Yang, L. Huang, P. Guo, B. Zhou, Y. Tao, C. Yang, Design, synthesis and performance control of dendritic fluorescent liquid crystal polymers with aggregation-induced emission properties, Eur. Polym. J. 186 (2023) 111855, https://doi.org/10.1016/j.eurpolymj.2023.111855.
[4] J. Li, J.H. Wang, X.J. Cao, X.D. Li, X.K. Ren, Z.Q. Yu, Peripherally modified tetraphenylethene: emerging as a room-temperature luminescent disc-like nematic liquid crystal, ACS Appl. Mater. Interf. 13 (2021) 35207–35213, https://doi.org/10.1021/acsami.1c10243.
[5] Q. Guo, M. Zhang, Z. Tong, S. Zhao, Y. Zhou, Y. Wang, S. Jin, J. Zhang, H.-B. Yao, M. Zhu, T. Zhuang, Multimodal-responsive circularly polarized luminescence security materials, J. Am. Chem. Soc. 145 (2023) 4246–4253, https://doi.org/10.1021/jacs.2c13108.
[6] F.-Y. Ye, M. Hu, C. Du, W. Yu, X.-P. Zhou, M. Liu, Y.-S. Zheng, Clear disclosure of hierarchical chirality transfer mechanism and wide full-color and white-light CPL emissions with both high glum and intensity by TPE helicates, Adv. Opt. Mater. 11 (2023) 2201784, https://doi.org/10.1002/adom.202201784.
[7] H. Feng, Y. He, W. Yang, S. Wang, Y. Feng, A novel strategy for constructing fluorescent liquid crystals with diphenylacrylonitrile groups derivatives based on Thiazolo[5,4-d]thiazole core, J. Mol. Struct. 1274 (2023) 134582, https://doi.org/10.1016/j.molstruc.2022.134582.
[8] W. Gong, G. Huang, Y. Yuan, H. Zhang, Strong and multicolor-tunable pure organic circularly polarized room-temperature phosphorescence from cholesteric liquid crystal, Adv. Opt. Mater. 11 (2023) 2300745, https://doi.org/10.1002/adom.202300745.
[9] W. Li, Y. Chen, Y. Ye, H. Guo, F. Yang, Triphenylene-fluorescein-triphenylene trimers: novel columnar liquid crystals with solid fluorescence, Liq. Cryst. 48 (2021) 1331–1338, https://doi.org/10.1080/02678292.2020.1864040.
[10] M. Czajkowski, Ł. Duda, S.J. Czarnocki, A.B. Szukalska, M. Guzik, J. Myśliwiec, M. Skoreński, B. Potaniec, J. Cybińska, Novel highly luminescent diketofurofuran dye in liquid crystal matrices for thermal sensors and light amplification, J. Mater. Chem. C Mater. 11 (2023) 4426–4438, https://doi.org/10.1039/d2tc04376a.
[11] S. Rani, S. Prasad Gupta, M. Gupta, S. Kumar Pal, Color-tunable photoluminescent discotic liquid crystal based on perylene – Pentaalkynylbenzene triad, J. Mol. Liq. 385 (2023) 122202, https://doi.org/10.1016/j.molliq.2023.122202.
[12] Y. Li, Y. Shen, K. Liu, Y. Quan, Y. Cheng, Tunable AI-CPL behavior by regulation of microstructure of AIE-active isomers through chiral emissive liquid crystals, Dyes Pigm. 186 (2021) 109001, https://doi.org/10.1016/j.dyepig.2020.109001.
[13] Y. Li, K. Yao, Y. Chen, Y. Quan, Y. Cheng, Full-color and white circularly polarized luminescence promoted by liquid crystal self-assembly containing chiral naphthalimide dyes, Adv. Opt. Mater. 9 (2021) 2100961, https://doi.org/10.1002/adom.202100961.
[14] P. Josse, K. Morice, D. Puchán Sánchez, T. Ghanem, J. Boixel, P. Blanchard, C. Cabanetos, Revisiting the synthesis of the benzothioxanthene imide five decades later, New J. Chem. 46 (2022) 8393–8397, https://doi.org/10.1039/d2nj00955b.
[15] P. Josse, S. Li, S. Dayneko, D. Joly, A. Labrunie, S. Dabos-Seignon, M. Allain, B. Siegler, R. Demadrille, G.C. Welch, C. Risko, P. Blanchard, C. Cabanetos, Bromination of the benzothioxanthene Bloc: toward new π-conjugated systems for organic electronic applications, J. Mater. Chem. C 6 (2018) 761–766, https://doi.org/10.1039/C7TC05245F.
[16] A. L. Dauphin, J. M. Andrés Castán, J. Yu, P. Blanchard, N. Sojic, H. S. Ahn, B. Walker, C. Cabanetos and L. Bouffier, Benzothioxanthene Dicarboximide as a Tuneable Electrogenerated Chemiluminescence Dye, ChemElectroChem 9 (2022) e202200967, DOI:10.1002/celc.202200967.
[17] L. Abad-Galán, J.M. Andrés Castán, C. Dalinot, P.S. Marqués, J. Galiana, P. Blanchard, C. Andraud, E. Dumont, O. Maury, C. Cabanetos, C. Monnereau, T. Le Bahers, Exploring the concept of dimerization-induced intersystem crossing: at the origins of spin-orbit coupling selection rules, J. Phys. Chem. B 125 (2021) 8572–8580, https://doi.org/10.1021/acs.jpcb.1c05082.
[18] D.J. Puchán Sánchez, P. Josse, N. Plassais, G. Park, Y. Khan, Y. Park, M. Seinfeld, A. Guyard, M. Allain, F. Gohier, L. Khrouz, D. Lungerich, H.S. Ahn, B. Walker, C. Monnereau, T. Le Bahers, C. Cabanetos, Driving triplet state population in benzothioxanthene imide dyes: Let’s twist!, Chem. Eur. J. (2024) e202400191.
[19] J. M. Andrés Castán, C. Amruth, P. Josse, L. Abad-Galán, P. S. Marqués, M. Allain, O. Maury, T. Le Bahers, P. Blanchard, C. Monnereau, G. C. Welch and C. Cabanetos, Thiochromenocarbazole imide: a new organic dye with first utility in large area flexible electroluminescent devices, Mater. Chem. Front. 6 (2022) 1912–1919. DOI: 10.1039/D2QM00299J.
[20] M. Deiana, J.D.S.M. Andrés Castán, P. Josse, A. Kahsay, D.P. Sánchez, K. Morice, N. Gillet, R. Ravindranath, A.K. Patel, P. Sengupta, I. Obi, E. Rodriguez-Marquez, L. Khrouz, E. Dumont, L. Abad Galán, M. Allain, B. Walker, H.S. Ahn, O. Maury,

P. Blanchard, T. Le Bahers, D. Öhlund, J. Von Hofsten, C. Monnereau, C. Cabanetos, N. Sabouri, A new G-quadruplex-specific photosensitizer inducing genome instability in cancer cells by triggering oxidative DNA damage and impeding replication fork progression, Nucleic Acids Res 51 (2023) 6264–6285, https://doi.org/10.1093/nar/gkad365.

[21] S.V. Dayneko, A.D. Hendsbee, J.R. Cann, C. Cabanetos, G.C. Welch, Ternary organic solar cells: using molecular donor or acceptor third components to increase open circuit voltage, New J. Chem. 43 (2019) 10442–10448, https://doi.org/10.1039/C9NJ01574D.

[22] J.M. Andrés Castán, C. Dalinot, S. Dayneko, L. Abad Galan, P.S. Marqués, O. Alévêque, M. Allain, O. Maury, L. Favereau, P. Blanchard, G.C. Welch, C. Cabanetos, Synthesis, characterization and use of benzothioxanthene imide based dimers, Chem. Commun. 56 (2020) 10131–10134, https://doi.org/10.1039/D0CC04556J.

[23] A. Merabti, D. P. Sánchez, A. Nocentini, L. M. A. Ali, C. Nguyen, D. Durand, K. Hamon, T. Ghanem, P. Arnoux, P. Josse, C. Frochot, R. Zalubovskis, S. Richeter, M. Gary-Bobo, C. T. Supuran, C. Cabanetos, J. Y. Winum and S. Clément, Thiochromenocarbazole imide-based photosensitizers decorated with carbonic anhydrase inhibitors for the targeted treatment of hypoxic tumours, Mater. Adv. (2024) Advance Article DOI:10.1039/d3ma00926b.

[24] M. Deiana, P. Josse, C. Dalinot, A. Osmolovskyi, P.S. Marqués, J.M.A. Castán, L. Abad Galán, M. Allain, L. Khrouz, O. Maury, T. Le Bahers, P. Blanchard, S. Dabos-Seignon, C. Monnereau, N. Sabouri, C. Cabanetos, Site-selected thionated benzothioxanthene chromophores as heavy-atom-free small-molecule photosensitizers for photodynamic therapy, Commun. Chem. 5 (2022) 142, https://doi.org/10.1038/s42004-022-00752-x.

[25] L. Krause, R. Herbst-Irmer, G.M. Sheldrick, D. Stalke, Comparison of silver and molybdenum microfocus X-ray sources for single-crystal structure determination, J. Appl. Crystallogr. 48 (2015) 3–10, https://doi.org/10.1107/S1600576714022985.

[26] G.M. Sheldrick, Crystal structure refinement with SHELXL, Acta Crystallogr. C Struct. Chem. 71 (2015) 3–8, https://doi.org/10.1107/S2053229614024218.

[27] C.B. Hübschle, G.M. Sheldrick, B. Dittrich, ShelXle: a Qt graphical user interface for SHELXL, J. Appl. Crystallogr. 44 (2011) 1281–1284, https://doi.org/10.1107/S0021889811043202.

[28] L.J. Farrugia, WinGX and ORTEP for Windows: an update, J. Appl. Crystallogr. 45 (2012) 849–854, https://doi.org/10.1107/S0021889812029111.

[29] C.F. MacRae, I. Sovago, S.J. Cottrell, P.T.A. Galek, P. McCabe, E. Pidcock, M. Platings, G.P. Shields, J.S. Stevens, M. Towler, P.A. Wood, Mercury 4.0: from visualization to analysis, design and prediction, J. Appl. Crystallogr. 53 (2020) 226–235, https://doi.org/10.1107/S1600576719014092.

[30] C.R. Groom, I.J. Bruno, M.P. Lightfoot, S.C. Ward, The Cambridge structural database, Acta Crystallogr. B Struct. Sci. Cryst. Eng. Mater. 72 (2016) 171–179, https://doi.org/10.1107/S2052520616003954.

[31] L. Fritsch, L.A. Baptista, I.H. Bechtold, G. Araújo, R.J. Mandle, A.A. Merlo, Isoxazoline- and isoxazole-liquid crystalline schiff bases: a puzzling game dictated by entropy and enthalpy effects, J. Mol. Liq. 298 (2020) 111750, https://doi.org/10.1016/j.molliq.2019.111750.

[32] S.A.A. Sanches, W.C. Costa, I.H. Bechtold, R.A.P. Halfen, A.A. Merlo, L.F. Campo, Bromine-terminated azobenzene liquid crystals, Liq. Cryst. 46 (2019) 655–665, https://doi.org/10.1080/02678292.2018.1517226.

[33] B. Yang, S. Yan, Y. Zhang, H. Ma, F. Feng and W. Huang, Cycloplatinated(II) metallomesogens and their binary-mediated chirality transfer and amplificated deep-red circularly polarized luminescence with ultrahigh dissymmetry factor over 0.13, Dyes Pigm. 221 (2024) 111813. DOI:10.1016/j.dyepig.2023.111813.

[34] R. Jiménez, F. Duarte, S. Nuti, J.A. Campo, C. Lodeiro, M. Cano, C. Cuerva, Thermochromic and acidochromic properties of polymer films doped with pyridyl-β-diketonate boron(III) complexes, Dyes Pigm. 177 (2020) 108272, https://doi.org/10.1016/j.dyepig.2020.108272.